The Astrophysical Journal Supplement Series, 267:23 (13pp), 2023 August https://doi.org/10.3847/1538-4365/acd9b4
© 2023. The Author(s). Published by the American Astronomical Society.
OPEN ACCESS

Vibrationally Resolved Absorption and Fluorescence Cross Sections of Adamantane in the Far-ultraviolet Spectral Range on an Absolute Scale

Lutz Marder[1], Alexander Breier[1], Nelson de Oliveira[2], Philipp Reiss[1], Philipp Schmidt[1,3], Christian Ozga[1], Catmarna Küstner-Wetekam[1], Thomas Giesen[1], Laurent Nahon[2], Andreas Hans[1], André Knie[1], and Arno Ehresmann[1]

[1] Institute of Physics and CINSaT, Universität Kassel, Heinrich-Plett-Str. 40, D-34132 Kassel, Germany; lutz.marder@physik.uni-kassel.de
[2] USynchrotron Soleil, Orme des Merisiers, St Aubin BP 48, F-91192 Gif sur Yvette Cedex, France
[3] UEuropean XFEL GmbH, Holzkoppel 4, D-22869 Schenefeld, Germany
Received 2022 November 2; revised 2023 April 27; accepted 2023 May 27; published 2023 July 20

Abstract

High-resolution absorption, dispersed fluorescence emission, and photoionization cross sections are presented for gas-phase adamantane excited by synchrotron radiation in the exciting-photon energy range of 6–30 eV. Relative and absolute absorption cross sections of so-far unmatched resolution of down to 0.27 cm^{-1} line width in the region from 6.4–28 eV are shown along with newly discovered vibronic substructures around the HOMO–LUMO transition. Absorption line positions are provided with very high accuracy and listed in tabular form to be used as spectral fingerprints for the detection of adamantane in interstellar media, where its column density may be determined via the absolute cross sections. The fluorescence emission lies in the ultraviolet range from 190–250 nm and is excited starting at the HOMO–LUMO transition at 6.49 eV, which corresponds to the highest fluorescence emission energy. Hitherto unreported fluorescence in the same spectral range and relative photoionization cross sections in the exciting-photon energy range up to 30 eV are also presented along with lifetime measurements for differentiation of the involved electronic states.

Unified Astronomy Thesaurus concepts: Ultraviolet surveys (1742); Ultraviolet spectroscopy (2284); High resolution spectroscopy (2096); Molecular spectroscopy (2095); Photoionization (2060); Interstellar molecules (849)

1. Introduction

Adamantane ($C_{10}H_{16}$) is the most stable isomer of a class of cycloalkanes and is discussed as a prospective material for nanostructures (McIntosh et al. 2004). It has, therefore, been the subject of extensive studies with the goal of unraveling its lattice structure, vibrational modes, energies (Shen et al. 1992; Jensen 2004; Filik et al. 2006; Patzer et al. 2012), and electronic structure (Korolkov & Sizova 2002). Adamantane is the smallest specimen of the diamondoids, a group of hydrocarbon molecules with a diamond-like structure due to the sp^3 hybridization of the outer carbon orbitals. It consists of a single closed-cage structure with surfaces terminated by hydrogen atoms; the larger diamondoids possess more cages. A detailed overview is given by Schwertfeger et al. (2008). In contrast to nanodiamonds, which may come in various sizes and structures extending up to several tens of nanometers in size, the size and structure of diamondoids are well defined.

In a study of electronically excited states in various cycloalkanes, photoabsorption of adamantane was first measured by Raymonda (1972) in the far-ultraviolet (FUV) or vacuum-ultraviolet (VUV) spectral range for photon energies between 6.4 and 9.5 eV. By comparing absorption features with energy levels calculated with the Rydberg formula, the lowest possible (HOMO–LUMO) electronic excitation at 6.49 eV and HOMO–LUMO+1 at 7.13 eV could be identified as 3*s*- and 3*p*-like Rydberg states. By using two-photon resonant, one-photon ionization spectroscopy, Shang & Bernstein (1994) measured photoelectron spectra with excitation energies of up to 10.5 eV and determined the $(\sigma 3s) \leftarrow (\sigma)^2$ transition to the molecular Rydberg state at 6.49 eV as well as higher vibrational states up to 6.7 eV. Several vibrational modes were identified using symmetry considerations.

In astrophysics, the findings of micro- and nanodiamond traces in meteorites by Lewis et al. (1989) posed questions on how and whether diamond-like material in interstellar media may be observed (see also Dartois 2019). It was discussed that absorption in the infrared (IR) spectral range due to nanodiamonds may not be very indicative due to the strong background of the interstellar medium. The detection by IR luminescence emission, moreover, is delicate because this emission might as well be caused by other hydrocarbons. In contrast, Allamandola et al. (1993) found a prominent IR feature that they attributed to a C–H stretching band in interstellar dense clouds, conjecturing the occurrence of diamond-like material there and contrasting to dominating spectral features of CH_2 and CH_3 groups in the diffuse interstellar medium. Although this conjecture is not completely unambiguous, it has been supported by theory (Duley 1995). It has sparked, moreover, investigations on the formation of diamonds in general in interstellar ices under UV radiation (Kouchi et al. 2005) and on diamondoids in particular by measured and calculated IR spectra for comparison with emission spectra from such interstellar clouds (see Bauschlicher et al. 2007; Pirali et al. 2007 and references therein), and the effect of ionization on these molecules (Polfer et al. 2004; Lenzke et al. 2007; Steglich et al. 2011; Patzer et al. 2012), as well as their stability. As a result, Bauschlicher et al. (2007) suspected that the diamondoids, if present in interstellar media,

Original content from this work may be used under the terms of the Creative Commons Attribution 4.0 licence. Any further distribution of this work must maintain attribution to the author(s) and the title of the work, journal citation and DOI.

exist in a neutral form, and their detection and identification are more promising by certain absorption features in the 3 m region rather than by emission because they are unlikely to be excited to emit strongly in the infrared. In contrast, Steglich et al. (2011) found that the photoionization of these molecules is very efficient given that a distinct broad peak in the photoionization yield exists at about 10.2 eV near the energy of hydrogen Lyα radiation. Using electronic photodissociation spectroscopy to investigate the adamantane radical cation, Crandall et al. (2020) found it to be too unstable to be a diffuse interstellar absorption band carrier, which was later confirmed by Kappe et al. (2022) in an extended survey on adamantane clusters and dehydrogenated adamantane in helium droplets. The complex dissociation dynamics of adamantane after double-ionization has recently been studied by Maclot et al. (2020) using XUV femtosecond pulses, where the process has been found to occur in two steps: a cage-opening, followed by fragmentation of the molecule.

Already Lewis et al. (1989) estimated that studying the absorption of UV/VUV photons may be more sensitive to the detection of diamond-like material in space. Also, the photon emission in this spectral range may be a good indicator. Fluorescence spectra in the ultraviolet after photoexcitation with synchrotron radiation of the lowest six diamondoids between 6 and 9 eV were measured both dispersedly and nondispersedly by Landt et al. (2009a) along with its photoabsorption. Highly resolved fluorescence spectra from triamantane to various pentamantanes were measured by Richter et al. (2015) after laser excitation with energies from 5.9–6.1 eV. The obtained spectra could be explained by Richter et al. (2014) in direct comparison to TDDFT-calculations for adamantane and in Richter et al. (2015) for larger diamondoids. These measurements showed a distinct, broad, and congested fluorescence in the range of 190–250 nm for all examined diamondoids and throughout the excitation energy range. The absorption spectra of the first six diamondoids and their isomers have been calculated by Vörös & Gali (2009) with the TDDFT method as a type of semiconductor nanoparticles, since absorption measurements for comparison were already available at the time (Landt et al. 2009b).

In a broad astrophysical perspective, complex organic materials, like adamantane, are chemical species formed only in specific environments best characterized by their UV/VUV spectrum and low temperature, such as the interstellar medium and some protoplanetary disks. In terms of astrobiological processes, the disks around young stars and their later evolutionary stages with possible icy bodies in planetary systems are perfectly suited objects to be investigated, too. The astronomical observation of specific tracer molecules can be done in emission or in absorption depending on the physical condition of the observed object. For more than 40 yr, the astronomical community used UV spectroscopy as a tool with great value through missions and instruments such as IUE (Macchetto & Penston 1978), the Hopkins UV Telescope (Davidsen & Fountain 1985), EUVE (Malina et al. 1982), HST-STIS (Kimble et al. 1997), FUSE (Sahnow et al. 2000), and HST-COS (Green et al. 2011). With only a few spectral high-resolution UV satellite missions flying until 2023, however, several future UV satellite projects have already been scheduled (SPARC; Jewell et al. 2018), are under construction (WSO-UV; Shustov et al. 2021), and/or are scheduled to successfully leave their conceptional phase soon (POLLUX; Muslimov et al. 2018). The idea of understanding the chemical evolution of the galaxy through a broad multi-spectral observation (Lebouteiller et al. 2019) requires the knowledge of numerous molecular fingerprints, from simple to complex molecular species, for their unambiguous identification and interpretation.

For astrophysical purposes, these characteristic UV emission and absorption spectra may be very useful as fingerprints alone or complementing IR spectra for a final clarification on the true abundance of diamondoids in space. Absolute cross sections for these species, however, were neither measured for emission nor for absorption with a reasonable accuracy up to now. In addition, to our knowledge, no spectra with exciting-photon energies above approximately 11 eV exist. Such absolute cross sections or even relative cross sections as a function of exciting-photon energy are essential for the determination of the density of a species in interstellar environments, which is why studies toward the determination of absolute cross sections have been performed extensively on molecular hydrogen, the most abundant molecule in the universe (see Glass-Maujean et al. 2010 and Schmidt et al. 2021, and references therein), and H_2O (see Hans et al. 2015 and references therein), and studies on relative cross sections for dispersed fluorescence emission as a function of the exciting-photon energy on several other small molecules, such as O_2 (Liebel et al. 2000, 2002; Ehresmann et al. 2004), NO (Ehresmann et al. 2003), and CO (Ehresmann et al. 2009).

Here, we examine the reaction of adamantane to the excitation by ultraviolet light below the ionization threshold using synchrotron radiation between 6.2 and 8.9 eV. In Section 3, a high-resolution absorption spectrum is presented with absolute cross sections. In Section 4, different fluorescence emission spectra in the same exciting-photon energy region are shown to explore the relaxation processes following the absorption. Then, as a survey above the ionization threshold, absolute photoionization and fluorescence emission in the excitation range from 6–30 eV, as well as relative total absorption cross sections up to 28.5 eV, are presented in Section 5.

2. Experimental Details

Results have been obtained during two experiments at synchrotron radiation facilities. The high-resolution absorption data in Sections 3 and 5 was measured with the VUV Fourier-transform spectrometer (VUV-FTS) at the DESIRS beamline (De Oliveira et al. 2011), located at the 2.75 GeV storage ring of the Synchrotron SOLEIL in France. DESIRS is a gas-phase UV–VUV beamline equipped with an HU640 undulator designed to offer high flux and variable polarization in the range between 4 and 40 eV (Nahon et al. 2012).

The remaining absorption, as well as the emission spectra, were measured using a home-built setup with single-photon counting position-sensitive photon detection (Hans et al. 2018) brought to the U125/2 10 m-NIM beamline (Reichardt et al. 2001) at the Helmholtz–Zentrum Berlin, BESSY II synchrotron facility. The U125/2 is a quasiperiodic undulator (Bahrdt et al. 2001), suppressing largely higher orders of the exciting photons. Therefore, this beamline is ideally suited for measurements of absolute cross sections with small uncertainties due to higher-order exciting-photon effects.

In the following two subsections, these experimental setups and the conditions at the synchrotron facilities will be briefly described.

2.1. High-resolution Absorption Spectroscopy with the VUV-FTS at SOLEIL

The VUV-FTS used for high-resolution absorption measurements is a permanent end-station on the VUV undulator-based beamline DESIRS at the SOLEIL synchrotron facility in France. It is built as a scanning wave front-division interferometer to overcome the problems involved with a regular beam splitter in the far-VUV range, since there exists no suitable transmitting material. The synchrotron radiation is directed into this beamline branch without further monochromatization, resulting in a so-called "pink" beam, a polychromatic Gaussian-shaped beam with a relative spectral bandwidth of around 7%, which can be used for the absorption measurements. Behind the beamline optics and the gas filter, which is used to get rid of high-energy photons from higher harmonic contributions, it is led through the gas sample environment chamber containing the target cell and surrounded by two differential pumping stages. We used two different target cells, an open one for relative absorption measurements and a windowed (MgF_2) one with an optical path length of 88.9 mm for absolute calibration. After passing the target cell and the subsequent interferometer, the transmitted synchrotron radiation is detected by a photodiode. The recorded interferograms are then post-processed and transformed into the absorption spectrum.

The commercially available solid-state adamantane sample is stored inside a glass reservoir outside the chamber, where it can be easily replaced or refilled without venting the chamber. The sample holder itself and the pipes connecting it to the target cell can be heated to reach the desired amount of vapor pressure for the measurement. The processing procedure of the measured data and further details on the VUV-FTS setup are explained in De Oliveira et al. (2011) and De Oliveira et al. (2016).

2.2. Fluorescence and Absorption Spectroscopy with the PIFS Setup at BESSY II

The setup for photon-induced fluorescence spectroscopy (PIFS) consists of a target cell inside an interaction chamber that is mounted on a McPherson 1 m normal-incidence spectrometer equipped with a 1200 lines mm^{-1} spherical grating blazed at 150 nm for dispersion of the fluorescence light (see Figure 6 in Hans et al. 2018) and an entrance slit width of 0.5 mm. The fluorescence was recorded using a single-photon counting, position- and time-resolving detector mounted also at 1 m distance on the exit arm of the spectrometer. In the used setup, at each grating position, a fluorescence wavelength interval of 27 nm can be detected with a spectral resolution of about 1.8 nm FWHM. The time resolution was determined to be 350 ps. A detailed description of the detector is given in Reiß et al. (2015) and Hans et al. (2018). Two metal apertures are mounted up- and downstream of the source volume of the fluorescence. Using a bias voltage of +10 V on one of these allows for the measurement of the photoion yield through the other aperture. The transmitted synchrotron radiation can be measured as a photocurrent at a photodiode downstream of the target cell.

For normalization purposes, the beamline's photon flux was recorded as a function of photon energy using a calibrated PtSi photodiode. This photodiode has a linear response over a wide intensity range (Solt et al. 1996), which avoids saturation effects during the intensity measurements. The bandwidth of the synchrotron radiation varied from 4 meV at 6 eV photon energy to 90 meV at 30 eV. In the recorded flux, an occasionally visible deviation of individual data points from the otherwise smooth function was compared to interpolated data points and led to an estimated uncertainty of 17% for the beamline flux.

3. Absorption below the Ionization Threshold

Absolute absorption cross sections were determined from 51,566 cm^{-1} (6.39 eV) to 72,037 cm^{-1} (8.93 eV) with a spectral resolution of 17.25 cm^{-1} (2 meV) using the VUV-FTS with a windowed target cell at SOLEIL. Before and after each measurement with the sample, a reference run with an empty cell was performed to account for possible shifts in the undulator spectrum. The vapor pressure of the sample has been controlled using a heating system wrapped around the sample holder and the tubes all the way up to the target cell. Depending on the spectral range, measurements were conducted with temperatures starting at room temperature up to 120 °C. Typical resulting pressures inside the target cell during the measurements were in the range of 0.1–0.3 mbar. A survey where we measured the same spectral region with different temperatures did not show a significant change in the measured absorption cross sections.

The windowed cell scans were recorded at room temperature with several different column densities for each spectral window and subsequently averaged in order to set an absolute value. The cross-section uncertainty is deduced by the general dispersion obtained and is estimated to be around 10%. The room-temperature windowless cell scans were scaled upon this absolute measurement, and the result is presented as the solid line in Figure 1. Line positions of the most prominent distinct features in the spectrum have been determined and are listed along with their corresponding absolute absorption cross sections in Table 1. A more comprehensive list also including weaker features and a description of the peak finding method can be found in Appendix A. More details concerning the FTS measurement procedure can be found in De Oliveira et al. (2016). Possible deviations of the recorded pressures to the actual adamantane vapor pressures, e.g., due to contaminants inside the glass reservoir, are difficult to estimate and would result in an underestimation of the true cross section. However, we assume this partial pressure to be of a relatively small magnitude, as we repeated a few identical spectral windows over the time of the experiment and did not find a significant deviation from the general statistical dispersion.

Clearly, in the frequency region from 52,300 cm^{-1} up to 55,500 cm^{-1} (see Figure 2), the excitation of adamantane is observable and reveals rovibrational features in the $(\sigma 3s) \leftarrow (\sigma)^2$ electronic transition toward a Rydberg state. This unique sequence of rovibronic transitions of adamantane in the UV region can be identified as a unique fingerprint for astronomical purposes fostering its clear detection in the interstellar environment. In the following paragraphs, the rovibronic features are investigated.

In this UV fingerprint region of adamantane, various spectral features are identified and classified into one strongly intense

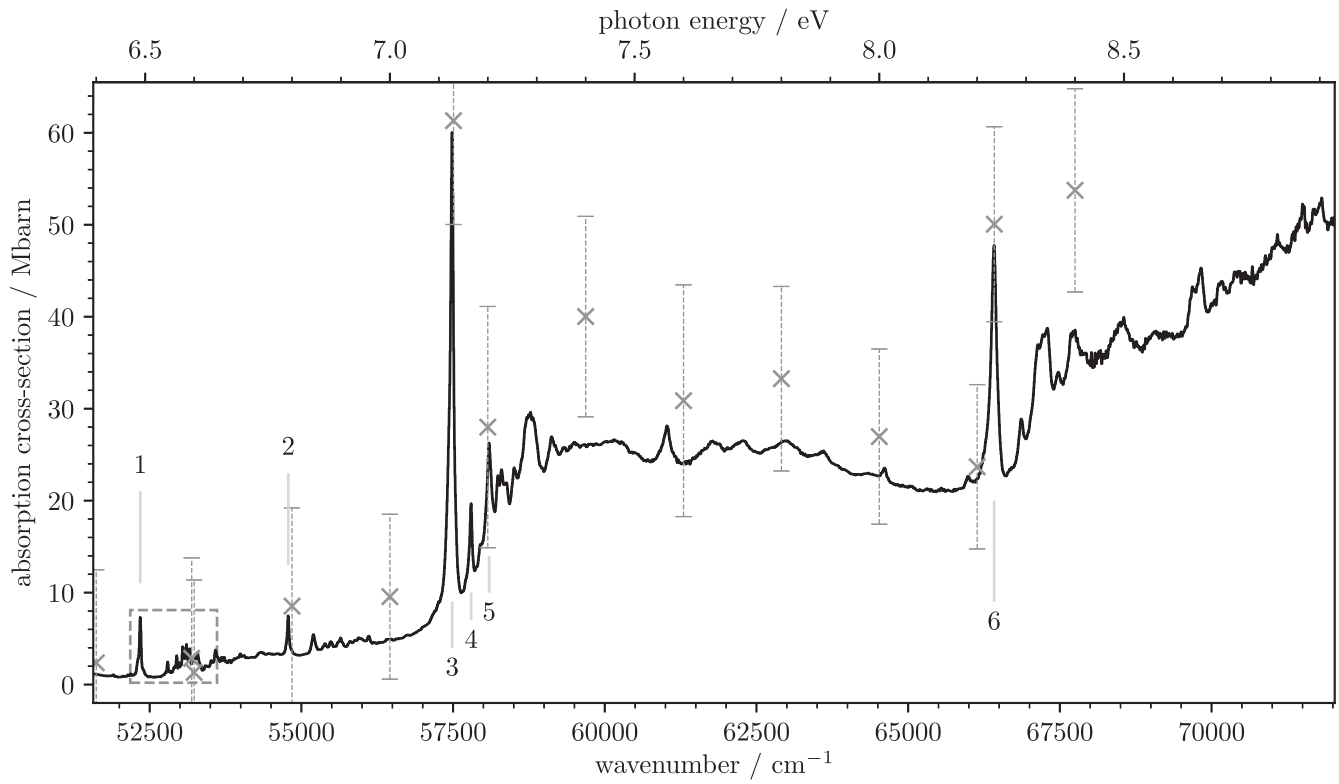

Figure 1. Absolute absorption cross sections for adamantane in the VUV spectral range below the ionization threshold. The distinct peaks at 6.49 eV, 7.13 eV, and 8.23 eV show the HOMO–LUMO, HOMO–LUMO+1, and +2 transitions. The data shown as a black line have been recorded with the VUV-FTS at SOLEIL and have an uncertainty of around 10% with a spectral resolution of 2 meV, the data shown as gray crosses have been recorded with the PIFS setup at BESSY II and analyzed independently to the Fourier-transform data. The framed region in the beginning is also shown in high resolution in Figure 2. See Table 1 for the positions of the most prominent lines in the spectrum.

Table 1
Most Prominent Distinct Features of Adamantane in the VUV Spectral Range below the IP between 54,000 cm^{-1} and 70,000 cm^{-1} (see Figure 1), the Corresponding Absolute Absorption Cross Sections and Excited States

	Line Position (cm^{-1}) ± 2.0	Abs. Cross Section (Mbarn) ± 10%	Exc. State
1	52,345	7.3	(σ 3s)
2	54,784	7.5	
3	57,486	60.0	(σ 3p)
4	57,798	19.7	
5	58,094	26.3	
6	66,417	47.8	(σ 3p)

Note. The line position statistical uncertainty was estimated to be below 2.0 cm^{-1}.

(1), six medium-intensity (2–7), and numerous weakly intense rovibronic transitions. The number of the observed medium-intensity transitions is quite similar to that from the experimentally observed vibrational modes up to 3000 cm^{-1} of the electronic ground state (compare Figure 2 in Pirali et al. 2012). The single most intense feature (1) is assigned to the fundamental transition 0_0^0 from the electronic ground state $(\sigma)^2$ into the (σ 3s) Rydberg state (HOMO–LUMO transition), located at 52,345.41(12) cm^{-1} and is in good agreement with the value obtained by Shang & Bernstein (1994). This fundamental vibronic transition is shaped by rotationally unresolved P-, Q-, and R-branches with a total spectral width of roughly 30 cm^{-1}. The widths of the branch structures are in good agreement with the observations from the fundamental IR modes (Pirali et al. 2012). About 4 cm^{-1} energetically higher located directly next to the main Q-branch of the fundamental transition lies an additional Q-branch feature, which is a known observation from the infrared measurements on adamantane (Pirali et al. 2012), contributed from several hot bands of the electronic ground state. Since these spectra have been recorded at around 100 °C, one can assume that the lowest vibrational states of adamantane are partly populated (Jensen 2004).

Initial attempts to reconstruct the shapes of the unresolved band structures of the more prominent features in the spectrum to reveal rovibronic transition shading were unsuccessful due to high complexity involving multiple branches per band center. In a simplified approach, we assumed only one P-, Q-, and R-branch per band center, which follows a normal distribution. For details on the shape reconstruction attempts and the peak finding procedure, see Appendix A. From this shape reconstruction, it follows that the center frequency of the broad Q-branch shape structure was suggested to be the band origin of the fundamental transition, leading to the value mentioned above.

The medium-intensity features of the UV fingerprint region are also structured by unresolved P-, Q-, and R-branch features, with a typical branch width of 20 cm^{-1}. For identification of the medium-intensity band centers, the simplified shape reconstruction method was used, and the results of these most prominent features in this region are listed in Table 2. The values of the medium-intensity features are in good agreement with the values obtained by (2+1') mass-resolved excitation spectroscopy by Shang & Bernstein (1994). The medium-

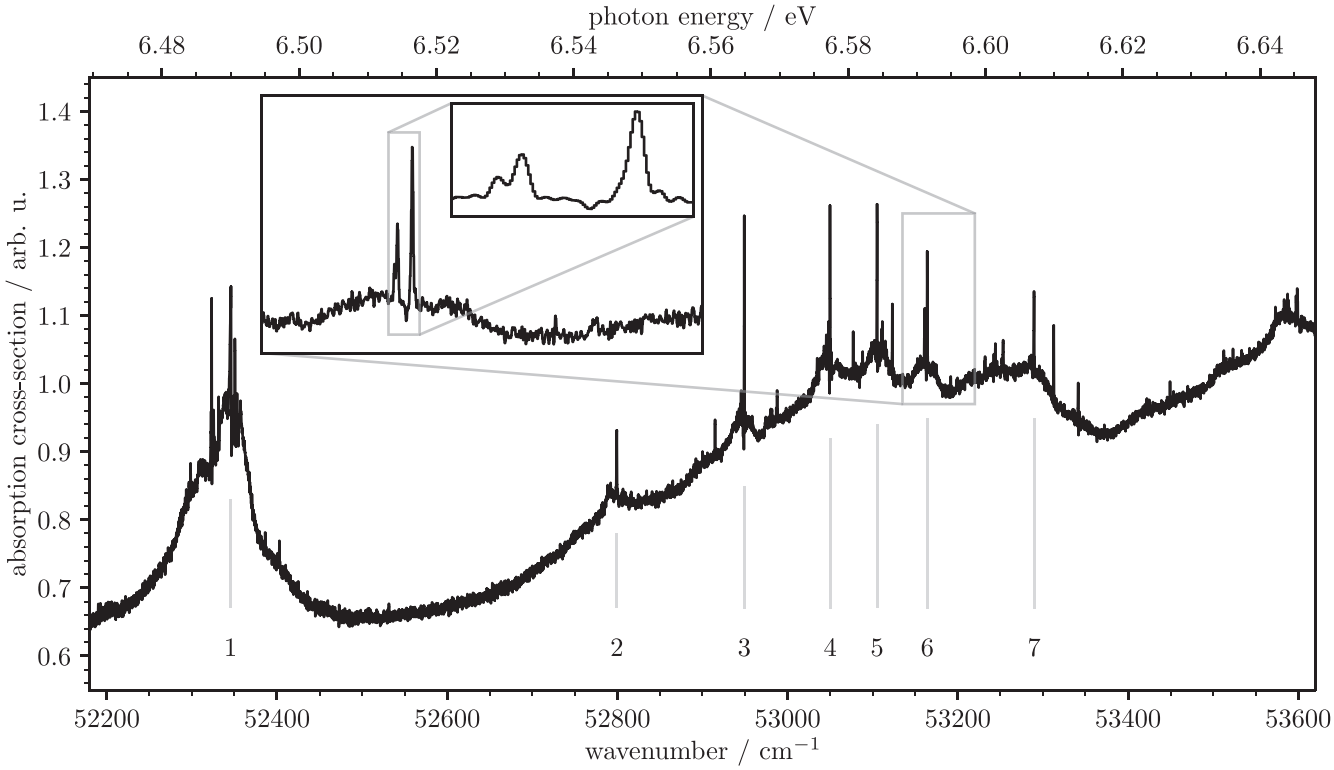

Figure 2. High-resolution (0.27 cm^{-1} or 0.03 meV line width) spectrum of rovibronic features in the absorption cross section for adamantane around the HOMO–LUMO transition at 6.49 eV, a zoom to one of the features (No. 6) exhibiting the typical branch structure and a farther zoom (showing a 6 cm^{-1} wide segment) to the sharp peaks. See Table 2 for the positions of the most prominent lines as numbered in the spectrum.

Table 2
Vibronic Features with Rotational Substructure of Adamantane between 52,300 cm^{-1} and 53,600 cm^{-1} (see Figure 2), the Corresponding Fundamental Modes, and Comparison with Reference Data from Shang & Bernstein (1994)

	Vibronic Feature	Fundamental Mode	Reference
1	52,345.41(12)		52358
2	52799.35(5)	453.94(13)	450
3	52949.11(6)	603.70(13)	600
4	53049.99(9)	704.58(15)	702
5	53105.12(10)	759.71(15)	760
6	53164.11(10)	818.70(15)	817
7	53289.59(6)	944.18(13)	943

Note. All values are given in cm^{-1}.

intensity vibronic features are identified as fundamental vibrational modes of the ($\sigma\,3s$) Rydberg state.

The weakly intense features are distributed over the whole UV fingerprint region from 52,300 cm^{-1} up to 55,500 cm^{-1}. No clear P- and R-branch structures can be observed here. The complete list of features in this region including the weakly intense ones can be found in Table 4. A clear identification of those transitions needs deeper experimental observation, so that also P- and R-branch structures are resolved, or/and theoretical guidance by anharmonic calculation upon the vibrational modes of the Rydberg states, which could help to properly assign the excited vibronic modes of adamantane.

The identification of the strongly intense and medium-intensity features in the UV region to vibronically excited adamantane results in a unique fingerprint and may lead in the future to an unambiguous detection in space by the astronomical community.

The most intense features in the full spectrum (see Figure 1) at 57,486 and 66,417 cm^{-1} belong to the 0-0 bands of Rydberg transitions into the ($\sigma\,3p$) excited states, whereas the transition at 52,345 cm^{-1} is the 0-0 band of the Rydberg transition into the ($\sigma\,3s$) (LUMO) state, as mentioned earlier. This has been found by Raymonda (1972) by calculation of the Rydberg series of adamantane, where quantum defects of 0.8 and 0.42—which lie in the typical ranges for s- and p-like orbitals, respectively—are optimal to reproduce these peaks. TD-DFT calculations performed by Vörös et al. (2011) confirm these findings, where further excitations with higher orders of angular momenta are also discussed. The sharper features at higher energies adjacent to the Rydberg peaks can probably be attributed to vibrationally excited states to the according Rydberg state, since they have been shown to also vanish when the Rydberg transition is suppressed, e.g., due to a perturber gas (Raymonda 1972). While the broad and mostly featureless region in the spectrum centered at around 62,000 cm^{-1} is attributed to $\sigma^* \leftarrow \sigma$ valence transitions by Raymonda (1972), newer findings suggest it (along with the increasing underlying background starting already at 53,500 cm^{-1}) to be the result of quantum nuclear dynamics (Patrick & Giustino 2013).

For consistency, a comparable measurement was performed with the PIFS setup at BESSY II. There, absolute absorption cross sections were determined from 6.4–8.4 eV in steps of 0.2 eV with a bandwidth of 4.6 meV and additionally at the two fixed energies of at 7.13 and 8.23 eV, where two distinct peaks —for the HOMO–LUMO+1 and +2 transitions—are present in absorption and fluorescence. Each energy step was measured with adamantane in the target cell, then with an empty cell, and then with the synchrotron beam shut off, for reliable

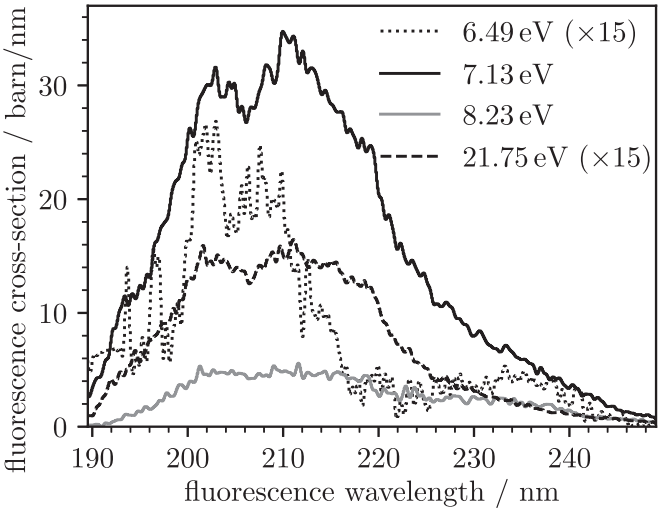

Figure 3. Dispersed fluorescence spectra of adamantane recorded at different exciting-photon energies. The spectra have been integrated over the emission wavelength range of 190–250 nm to obtain their total emission cross sections (see the text).

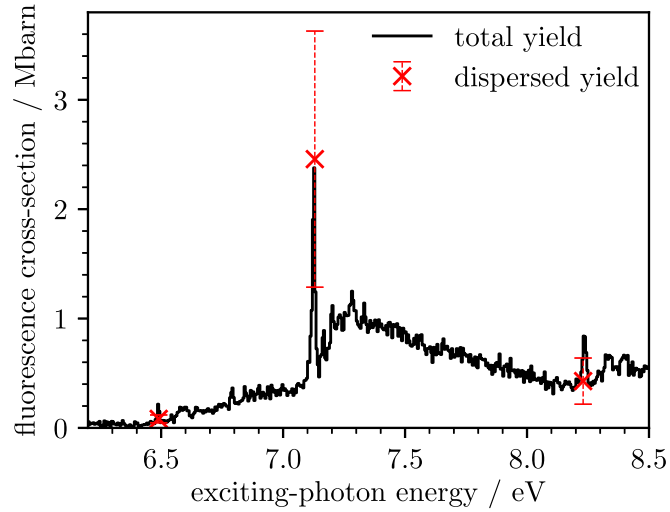

Figure 4. Total UV fluorescence cross sections for adamantane in the exciting-photon energy range from 6.2–8.5 eV with an uncertainty of around 15%. Shown also are the obtained cross sections from dispersed measurements in first order that have been used for scaling the zeroth-order data for the best fit. The peak at 6.49 eV corresponds to the HOMO–LUMO transition, the ones at 7.13 and 8.23 eV to HOMO–LUMO+1 and +2, respectively. The large number of peaks in between can be attributed to excited vibrational states of these transitions.

background determination. Every setting was measured six times over the course of 60 s with each data point being averaged over 10 s. The absorption cross sections were then calculated via the Lambert–Beer law including corrections for preabsorption due to sample leakage and thereby an increase in the effective optical pathway, uncertainties in the cell geometry, and a systematic shift due to heat-up effects (for details, see Appendix B) with the values shown in Figure 1 (gray crosses) corresponding to the mean values of these repeated measurements. Considering the error bars, the measurements performed with the PIFS setup are in good agreement with the spectrum acquired with the VUV-FTS.

4. Photon Emission below the Ionization Threshold

After observing the absorption features, the question arises of how these rovibronically excited states relax afterwards. With excitation energies below the ionization threshold of adamantane, it is safe to assume the relaxation to happen radiatively or via neutral dissociation. Here, we focused on the former and performed follow-up measurements using the PIFS setup at BESSY II to investigate fluorescence processes after excitation with synchrotron radiation at four different energies. The recorded dispersed spectra are then normalized and calibrated to an absolute scale using known values for cross sections of nitrogen (for details, see Appendix C). The obtained spectra and fluorescence emission cross sections at exciting-photon energies of 6.49 eV (corresponding to the bandgap or HOMO–LUMO transition), 7.13 eV (HOMO–LUMO+1), 8.23 eV (HOMO–LUMO+2), and 21.75 eV (above ionization threshold) are presented in Figure 3. For these energies, the determined fluorescence cross sections integrated over the emission wavelength range between 190 nm and 250 nm are 78 ± 40 kbarn, 2320 ± 1277 kbarn, 403 ± 228 kbarn, and 26 ± 10 kbarn, respectively.

Additionally, the lifetimes of the excited states were investigated. For the HOMO–LUMO transition, they have already been determined in Richter et al. (2014). To measure the lifetimes of the transitions at 7.13, 8.23, and 21.75 eV, we first performed a calibration with scattered light that included only the width of the synchrotron pulse and the time resolution of the apparatus, which was determined as a Gaussian with an FWHM of 0.35 ns. The measurement of each excited state lifetime was then fitted as a convolution of the Gaussian with an exponential decay. The resulting lifetimes are 1.34 ± 0.03 ns, 1.00 ± 0.02 ns, 0.48 ± 0.02 ns, and 7.09 ± 0.29 ns, respectively. The decrease in lifetime with higher excitation energies can be explained by an increase of decay pathways from the larger amount of vibrational transitions and with the shorter lifetime of the energetically higher ($\sigma 3p$) state compared to ($\sigma 3s$). The comparatively high lifetime at 21.75 eV might be the result of a cascade process.

All dispersed spectra show an unresolved manifold of fluorescence lines between 190 nm and 250 nm, which is already known from Landt et al. (2009a) and Richter et al. (2014). Outside this wavelength range, only negligible intensity was recorded with the present spectrometer/detector combination. These lines originate from the transition between vibrational excitations from 72 normal vibrational modes and their overtones between the excited $\sigma 3s/\sigma 3p$ states and σ^2 ground state. In the spectrum at 6.49 eV, scattered light from the synchrotron beam was visible around approximately 192 nm, which was removed from the spectrum and disregarded in the integration for the cross section. This effect is also visible in the results from Richter et al. (2015). The spectrum at 21.75 eV is remarkable because its excitation energy is far above the ionization potential of 9.23 eV (Lenzke et al. 2007), yet it is similar to the other fluorescence spectra.

For the determination of total absolute fluorescence emission cross sections in the present wavelength range as a function of exciting-photon energy, undispersed fluorescence has been recorded by setting the spectrometer to zeroth order. The background was collected with an empty target cell in the same way and subtracted from the spectrum. The normalized fluorescence was scaled to the cross sections from the dispersed measurements. Figure 4 displays the corresponding result recorded for the exciting-photon energy range between 6.2 and

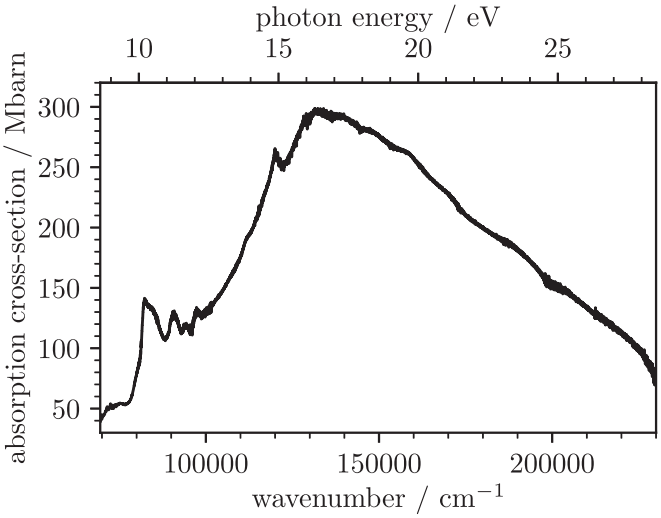

Figure 5. Absolute absorption cross section for adamantane above the ionization threshold. The uncertainty is estimated to be around 20%. The alleged features in the right region are artifacts of the merging process of different individual spectra of smaller intervals.

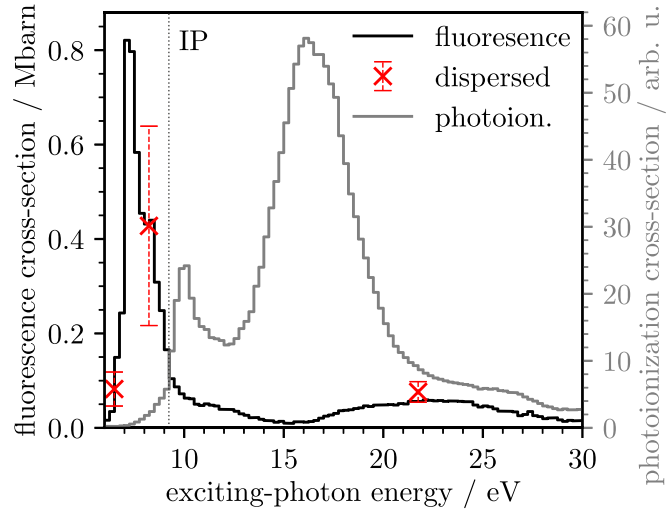

Figure 6. Total UV fluorescence excitation function and photoionization cross sections for adamantane in the exciting-photon energy range from 6–30 eV. Uncertainties are estimated to be around 20% for both the fluorescence excitation function and the photoionization cross sections. The ionization threshold (IP) and the obtained cross sections from dispersed measurements that have been used for scaling the zeroth-order data for the best fit are also shown.

8.5 eV at a bandwidth of 5.3 meV, and the uncertainty is estimated to be around 15%.

Calculations by Richter et al. (2014) show that most of the peaks in the spectrum are not necessarily single, strong transitions, but rather the sum of several weaker transitions in close proximity that have not been resolved; exceptions are intense Rydberg excitations to a vibrational ground state such as the peaks at 6.49 eV and 7.13 eV.

The rather large difference between the absorption and UV fluorescence cross section is indicative of other relaxation pathways. Among others, typical processes in a molecule like adamantane include neutral dissociation into either nonexcited or weakly excited fragments, vibrational relaxation, and internal conversion; a possible remaining excitation could then lead to the emission of photons of lower energies than measured in this experiment. A fluorescence cascade via an intermediate excited state might also not be detected here.

5. Absorption, Fluorescence, and Photoionization above the Ionization Threshold

In addition to the examinations of adamantane in the region below its ionization threshold, we have extended the investigation to the exciting-photon energy range up to 28.5 eV. Due to the lack of transparent materials for photons in this energy region, measurements could only be performed using a windowless cell and thus without a defined optical path length, preventing the possibility of direct absolute calibration of the data. Hence, relative cross sections have been measured using the VUV-FTS setup at SOLEIL and calibrated to an absolute scale using the spectrum below the threshold (Figure 1), resulting in the spectrum presented in Figure 5. The absolute absorption cross section is propagated from the lower toward the high-energy spectral range by connecting the individual overlapping spectral windows, which form the full spectrum when merged together. The width of the intervals is given by the spectral range of the radiation produced by the undulator. These VUV-FTS spectral windows could suffer a small asymmetry that would translate into an extra uncertainty on the absolute calibration. Note that this effect increases with the photon energy; this phenomenon was described in detail in De Oliveira et al. (2016). By examining the general overlap between spectral windows, we have estimated a maximum uncertainty of 20% above the IP for the absolute cross section by considering the overall causes identified.

In this spectral region, the FTS interferometric signal is much more sensitive to external perturbation, which makes the background subtraction and subsequent merging less accurate and leads to some broad but weak artifacts in the spectrum; see De Oliveira et al. (2016) for details. The spectrum shows prominent features around 10.2, 11.2, 12, and 14.9 eV, and a broad hump between 13 and 25 eV with its maximum at 16.5 eV. Simulations by Steglich et al. (2011) show very similar structures in the absorption cross section that are attributed to σ–σ^* excitations. Their computed spectrum is dominated by a broad feature with a maximum between 15 and 20 eV and shows several peaks, e.g., at 8, 9, 11, and 12.5 eV, which is in good agreement with our measurements. The region above 15 eV is assumed to be one very broad feature without significant substructure, as far as can be deduced by our measurements.

As in Section 4, an interesting follow-up issue is now the adamantane molecule photodynamics in this energy range. Thus, in addition to the highly resolved fluorescence measurements (Figure 3), total fluorescence emission cross sections have been determined using the PIFS setup in a wider exciting-photon energy range from 6–30 eV along with a measurement of the photoionization yield. The bandwidth was 5.3 meV on the low-energy side and increased up to 85 meV on the high-energy side of the scan. Earlier measurements of the fluorescence emission (Raymonda 1972; Steglich et al. 2011; Richter et al. 2014) did not exceed the exciting-photon energy of 10.5 eV due to technical reasons in the respective setups, such as the transmitting range of MgF_2 windows. To our knowledge, experiments at higher exciting-photon energies have not yet been performed. Figure 6 shows the obtained photoionization and fluorescence cross sections. The (adiabatic) ionization potential from Lenzke et al. (2007) at 9.23 eV

as well as the fluorescence cross sections from the dispersed measurements are also included in the image. The photocurrent scattered during the measurement and caused a comparatively large statistical error of the relative photoionization cross sections of around 20%, and the fluorescence excitation function has a similar uncertainty of also around 20%. Another contribution to the uncertainty and the reason for a spurious photoionization signal below the ionization threshold is synchrotron radiation of higher orders, which is partially, but not fully, suppressed by the quasiperiodic undulator. The adamantane vapor pressure is measured using a capacitance manometer at the gas line outside the vacuum; the uncertainty due to these readings is assumed to be less significant than the other contributions, but is also taken into account.

The fluorescence excitation spectrum shows the already known features in the range up to 9 eV, where the intensity drops at the ionization threshold until it reaches a minimum at 15.5 eV, only to rise again in a broad, so-far undocumented feature that stretches to around 30 eV.

The photoionization cross section shows two distinct maxima at approximately 10.2 and 16.5 eV. Steglich et al. (2011) commented that the first ionization maximum is very close to the energy of the Lyα emission of hydrogen (10.2 eV) and so that photoionization should be a very efficient process in interstellar media, which then usually leads to a dehydrogenated adamantyl cation. The peak at 16.5 eV has not been measured so far. Both features can also be found in the absorption cross section shown in Figure 5. The simulated spectrum by Steglich et al. (2011), as already discussed above, shows a very similar structure in the absorption cross section, which is attributed to the collective σ–σ^* excitation. Subsequent autoionization processes lead to the respective features in the ion yield. Note that other sharp features from the absorption cross section possibly exist in the ion yield as well, but could not be resolved in the measurement. Photoelectron spectra and binding energies from Tian et al. (2002) suggest that, with increasing photon energy, inner-valence electrons are ionized and contribute to the total photoionization yield. The origin of the 16.5 eV centered structure could also lie in a shape resonance in the outer-valence shell ionization channels. Confirmation would require theoretical modeling, which is beyond the scope of the present paper.

Due to the occurrence of fluorescence with a cross section of approximately 50 kbarn at about 20 eV in the present measurement (Figure 6), another dispersed measurement was performed at the exciting-photon energy of 21.75 eV, which corresponds to the intensity maximum of the beamline. This fluorescence spectrum resembles closely those that have been found in excitations below the ionization threshold as shown in Figure 3. A possible reason for this is the formation of excited adamantyl cations and their following relaxation.

Analogous to the results below the threshold, there is a significant difference between the measured absorption and UV fluorescence cross section. A large part of this can obviously be attributed to direct photoionization, but there is also expected to be a variety of further relaxation channels, among others again vibrational relaxation and internal conversion, possibly leading to fluorescence in a different wavelength regime. For a complete overview of decay pathways, further investigation using different experimental setups would be required and is far beyond the scope of this work.

6. Conclusions

Fluorescence emission and absorption cross sections of gas-phase adamantane on an absolute scale were presented for the first time, along with photoionization cross sections on a relative scale.

Below the ionization threshold, absolute absorption cross sections have been measured starting at 6.39 eV, below the HOMO–LUMO transition, up to 8.93 eV, slightly below the ionization threshold, with uncertainties in the range of 10% and a spectral resolution of 0.002 eV. The data can be used as a parameter for modeling absorption spectra for astrophysical purposes and as an accurate fingerprint for the occurrence of adamantane, and its quantification, in the ultraviolet spectral range, as opposed to the infrared regime, where spectra of other hydrocarbons make a distinction much more difficult. The relative absorption and photoionization cross sections between 9 eV and 30 eV may be used for the same purpose and as a means for estimating the degree of ionization that can be expected in interstellar environments.

Fluorescence emission cross sections in the exciting-photon range between 6.2 and 8.5 eV are also presented. These spectra give insight into the mechanism of excitation and de-excitation between numerous vibrational states and their symmetries. Dispersed fluorescence at exciting-photon energies of 6.49, 7.13, 8.23, and 21.75 eV (HOMO–LUMO+0, +1, +2, and above the threshold) was measured as well along with the lifetimes of the corresponding excited states. The fluorescence above the threshold has been found to have a distinctly higher lifetime but a very similar shape compared to the other spectra, which might be an indication of a cascading relaxation process.

Furthermore, the model system adamantane is suited perfectly to be a benchmark test for state-of-the-art ab initio calculations due to its large number of atoms and its corresponding degrees of freedom within the molecular frame. The experimentally resolved vibrational states on the excited state in high resolution provide a perfect test bed for modern calculations.

Acknowledgments

This work was supported by the State Initiative for the Development of Scientific and Economic Excellence (LOEWE) in the LOEWE-Focus ELCH and the Federal Ministry of Education and Research, as well as the subsequent SFB 1319 ELCH, funded by the Deutsche Forschungsgemeinschaft (DFG; project No. 328961117). The support is gratefully acknowledged.

The authors thank HZB and SOLEIL for the allocation of synchrotron radiation beam times and the latter also for access to the VUV-FTS end-station at the DESIRS beamline under project No. 20181786. Finally, we thank Tobias Zimmermann, Robert Richter, and Thomas Möller for providing calibrated flux data of the U125/2 10m-NIM beamline.

Appendix A
Positions of Distinct Absorption Features of Adamantane in the VUV Spectral Range

In a first attempt, the investigation of the fundamental transition 0_0^0 from the electronic ground state $(\sigma)^2$ into the $(\sigma\, 3s)$ Rydberg state (No. 1 in Figure 2) is guided by a shape reconstruction of the unresolved band structures aiming to reveal the rovibronic transition shading. Therefore, the band

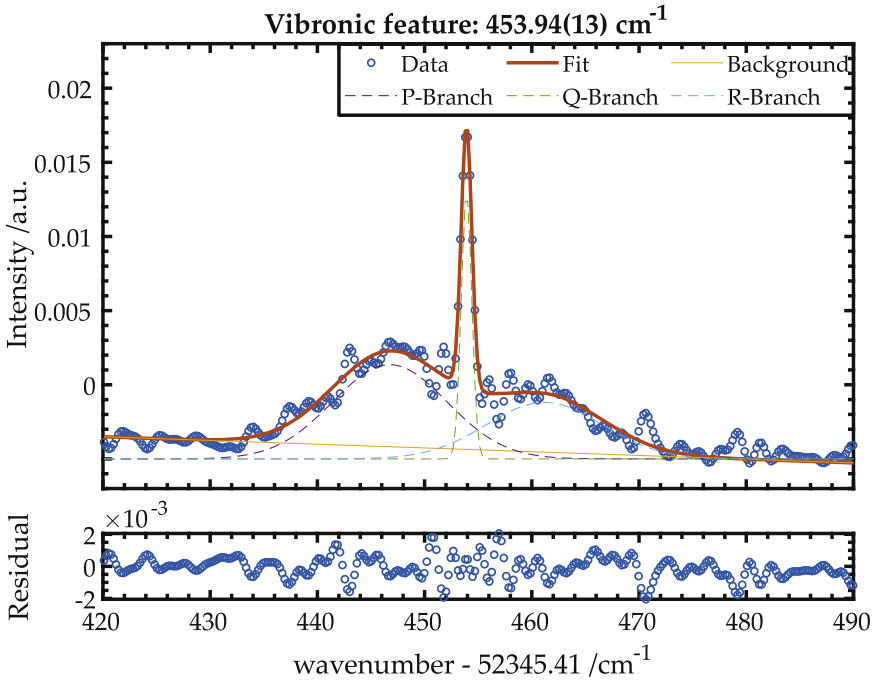

Figure 7. An exemplary triple-Gaussian fit to one of the features (No. 2) of the highly resolved spectrum shown in Figure 2. The result for the Q-branch position (with respect to the fundamental mode) of 453.94(13) cm^{-1} includes uncertainties for this feature's position and for the fundamental mode's position. Note that for clarity, not all measured data points are shown in this comparatively broad spectral window.

shapes are assumed to follow a skewed normal distribution. During the first fitting step, only one P-, Q-, and R-branch is assumed, revealing that a second Q-like branch feature is needed to reduce the contour fitting residual, being 4 cm^{-1} energetically higher located next to the main Q-branch. In the next fitting step, several additional Q-like branch features on the P- and R-branch are needed to further reduce the contour fitting residual. The number of additional Q-branch shapes changes the conclusion about the shading of the fundamental transition. Therefore, the attempt to obtain shading information from shape reconstruction was dropped. By a coarser investigation, the identification of the band center was simplified by assuming only one P-, Q-, and R-branch that follows a normal distribution. From this coarse shape reconstruction view, it follows that the center frequency of the Q-branch shape was suggested to be the band origin of the fundamental transition, leading to the value 52,345.41(12) cm^{-1}.

Most attempts to reconstruct the shape of the medium-intensity features (Nos. 2–7 in Figure 2) by skewed normal distributions also led to the demand for several Q-branch-like features. Hence, the medium-intensity band centers were also identified using the simplified shape reconstruction method (see Figure 7 for an example), and the results of these most prominent features in this region are listed in Table 2.

The weakly intense features are distributed over the whole UV fingerprint region from 52,300 cm^{-1} up to 55,500 cm^{-1}. No clear P- and R-branch structures are observed, and therefore, no band centers could be determined this way. Instead, we regarded them as single sharp peaks and determined the positions by assuming common Gaussian line shapes.

Figure 8 shows an exemplary fit to a typical weak feature in the high-resolution spectrum (see Figure 2), which yielded a peak position of 52914.831(6) cm^{-1} and an FWHM of

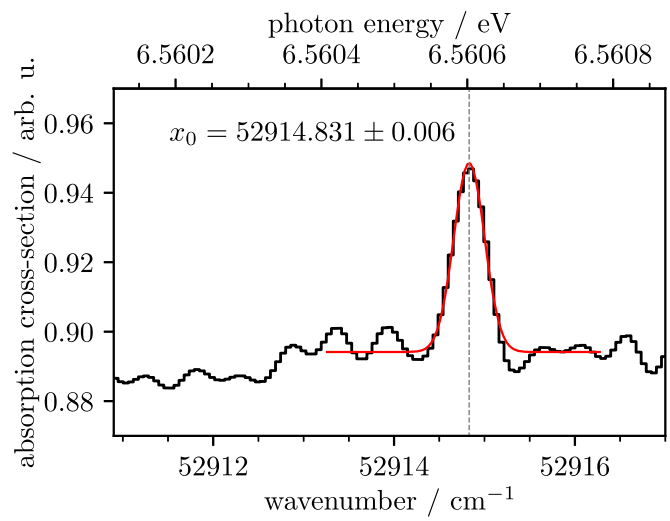

Figure 8. An exemplary Gaussian fit to one of the weak features of the highly resolved spectrum shown in Figure 2. The black curve is the measured absorption spectrum, the red one is the Gaussian fitted to an interval around and including the peak. The dashed line indicates the determined peak position x_0.

0.401(15) cm^{-1}. The uncertainty of the peak position can also be calculated for the FTS measurements from the respective FWHM, the signal-to-noise ratio (S/N), and the number of measured points N forming the peak, using the formula

$$\Delta\sigma = \frac{2}{\sqrt{N}} \frac{\mathrm{FWHM}}{\mathrm{S/N}}, \tag{A1}$$

which provides an empirical estimation for the statistical precision (Brault 1987). The uncertainty given above by the standard deviation of the fitting procedure is consistent with the estimated precision using this formula, which is, for this example, $\Delta\sigma \approx 0.01$ cm^{-1} (with $N = 16$, S/N= 20). The total

uncertainties of the determined positions are, in all cases, dominated by the accuracy of the measured data, which is estimated to be below 0.15 cm^{-1} for the high-resolution measurement and 2.0 cm^{-1} for the full spectrum. The different contributions to the total uncertainty are discussed in more detail in De Oliveira et al. (2011) and De Oliveira et al. (2016).

As a result, Table 3 shows a list of all sharp features found within the examined VUV spectral range as depicted in Figure 1, excluding the fundamental vibrational modes of the ($\sigma 3s$) Rydberg state in the lower-energy region. The latter are presented in Table 4 as a complete list of all unambiguous features in the respective spectral window as shown in Figure 2.

Table 3

Distinct Features of Adamantane in the VUV Spectral Range below the IP between 54,000 cm^{-1} and 70,000 cm^{-1} (see Figure 1), the Corresponding Absolute Absorption Cross Sections and Their Qualitative Intensities (Strong, Medium, Weak, Very Weak) with Respect to the Continuous Background

	Line Position (cm^{-1}) ± 2.0	Abs. Cross Section (Mbarn) ± 10%	Rel. Intensity
1	52,345	7.3	m
2	54,784	7.5	m
	55,200	5.5	w
3	57,486	60.0	s
4	57,798	19.7	m
5	58,094	26.3	m
	58,242	22.7	w
	58,300	23.4	w
	58,383	21.9	vw
	58,507	23.6	vw
	59,125	27.0	vw
	61,026	28.1	w
	64,612	23.6	vw
	65,989	22.7	vw
6	66,417	47.8	s
	66,865	28.9	w
	67,478	34.0	vw
	69,687	43.3	vw
	69,828	45.3	w

Table 4

Vibronic Features with Rotational Substructure of Adamantane between 52,300 cm^{-1} and 53,600 cm^{-1} (see Figure 2) Given as Fundamental Modes with Respect to the Origin at 52,345.4 cm^{-1}, Their Relative Intensities, and Comparison with Reference Data from Shang & Bernstein (1994), if Present

	Fundamental Mode (cm^{-1}) ± 0.15	Rel. Intensity	Reference (cm^{-1})
1	0	s	0
2	453.9	m	450
	470.5	vw	
	554.7	vw	554
	569.3	w	568
	600.0	w	
3	603.7	s	600
	635.4	vw	634
	642.2	w	
	689.3	w	
4	704.6	m	702
	731.5	w	730
	742.8	vw	
5	759.7	m	760
	765.8	w	764
	777.6	w	776
	815.7	w	
6	818.7	m	817
	846.2	vw	
	853.6	vw	853
	886.3	vw	885
	896.8	vw	897
	898.6	vw	
	907.7	w	907
	911.3	vw	912

Table 4
(Continued)

	Fundamental Mode (cm^{-1}) ± 0.15	Rel. Intensity	Reference (cm^{-1})
7	944.2	m	943
	967.2	m	
	995.9	w	994
	1076.6	vw	1071
	1079.5	vw	
	1103.8	vw	1103
	1107.8	vw	
	1167.1	vw	
	1177.8	vw	1176
	1188.0	vw	1187
	1197.3	vw	
	1227.7	vw	1227
	1238.0	vw	
	1242.0	vw	1241
	1253.3	w	1256
	1282.5	vw	

Note. The line position statistical uncertainty was estimated to be below 0.15 cm^{-1} for all listed features.

Appendix B
Evaluation Method for Absolute Absorption Cross Sections from PIFS Measurements

From the relative absorption, which has been detected using the PIFS setup, the absolute absorption cross sections have been calculated via the Lambert–Beer law using the optical pathway and the particle density. The resulting values showed an offset of -32 Mbarn, which is assumed to be a result of the measurement procedure, where measurements with a sample in the target cell were performed after a measurement without a synchrotron beam for every data point. A heat-up effect of the last refocusing mirror is assumed to be the reason for the systematic measurement deviation as well as the large uncertainty margins. The offset was corrected by using an earlier absorption measurement from Landt et al. (2009a), which was on a relative scale yet with a defined zero line. Both the scaling factor that puts these relative values to an absolute scale and the offset for the present data were calculated by performing a linear regression between the values of both data sets. The uncertainty margins for the calculated cross sections contain the standard deviation of the recorded values, the uncertainty of the absorption length, and the uncertainty of the offset value.

During the measurement, gaseous adamantane leaked out of the target cell at its entrance into the direction of the synchrotron beam. This contributed to the absorption signal not being considered in the absorption length of the used cell of 21.8 mm. This preabsorption is considered with equations from Sharipov & Seleznev (1998). The opening of the target cell into the vacuum of the target chamber consists of the orifice in the ion yield aperture with a radius of 1.5 mm, then a cannula with a radius of $r_c = 4.8$ mm and a length of $l_c = 18.2$ mm. By Equation (4).3 in Sharipov & Seleznev (1998), the number N of adamantane molecules with mass $m = 136.23$ u, temperature $T = 296$ K, and the pressure in the target cell $p_{tc} = 6.03$ Pa that passes through the orifice with radius o out of the cell per time t is

$$\frac{N}{t} = p_{tc} \cdot o^2 \cdot \sqrt{\frac{\pi}{2mk_B T}} = 5.590 \cdot 10^{17}\ s^{-1}. \quad (B1)$$

The adamantane molecules pass through the ion yield aperture into the cannula with a mean velocity in the direction of the cannula v_c following Equation (4.1) by Sharipov & Seleznev (1998)

$$v_c = \sqrt{\frac{2k_B T}{\pi m}} = 107.23\ m\ s^{-1} \quad (B2)$$

and, thus, pass the cannula length l_c within $t_c = 1.7 \times 10^{-4}$ s. In this time, 9.5×10^{13} molecules flow into the cannula out of the target cell and an equilibrium is formed between the rates of entering and exiting molecules. This number of molecules within the volume of the cannula corresponds to a particle density of 7.2×10^{19} m^{-3}, which itself corresponds to a pressure of $p_c = 0.29\ Pa = 0.048 \cdot p_{tc}$. As a result, an additional absorption length of $l_c \times 0.048 = 0.9$ mm is added to the geometrical length of the cell itself. An uncertainty of 2 mm that stems from the assembly of the cell is also included in the calculation of the absorption cross section. It is assumed that the density outside of the cannula in the experimental chamber is negligible.

Appendix C
Normalization and Evaluation Method for Absolute Fluorescence Cross Sections

For fluorescence detection, a position-sensitive detector (see Reiß et al. 2015; Hans et al. 2018) was used. Therefore, not only the spectral but also the position-dependent (lateral) quantum efficiency $QE_{lat}(x, y)$ has to be determined. This was achieved by setting the beamline energy to 6.89 eV (180 nm), introducing a mixture of nitrogen and oxygen at a pressure of 20 Pa into the target cell, and measuring the intensity of the

elastically scattered synchrotron light as a function of its position on the detector surface. The position was changed by rotating the optical grating of the fluorescence spectrometer. All of the following spectra were then normalized for this lateral quantum efficiency with an uncertainty margin of 0.8%. The lateral quantum efficiency has been assumed to not change for other wavelengths within the given uncertainty.

The relative spectral quantum efficiency of the detector/grating combination $QE(\hbar\omega)$ was measured again with elastically scattered light from the synchrotron. As the fluorescence lines used for calibration to absolute cross sections are in the range between 120 nm and 150 nm, and the adamantane emission is around 210 nm, $QE(\hbar\omega)$ is an important quantity. The beamline energy was scanned from 4 eV (310 nm) to 11 eV (113 nm), and intensities were recorded in both zeroth and first order of diffraction of the spectrometer. The resulting intensity curves $I_{0,1}(\hbar\omega)$ are the product of the spectral and lateral quantum efficiencies of the setup and the flux of the beamline $I_{0,1}(\hbar\omega) = QE_{0,1}(\hbar\omega) \cdot F(\hbar\omega) \cdot QE_{\mathrm{lat}}(x, y)$. To obtain the quantum efficiency, this curve was divided by the measured beamline flux and the lateral quantum efficiency $QE_{0,1}(\hbar\omega) = I_{0,1}(\hbar\omega)/(F(\hbar\omega) \cdot QE_{\mathrm{lat}}(x, y))$. The obtained quantum efficiency $QE_{0,1}(\hbar\omega)$ possesses uncertainty margins of 19% and is dominated by the uncertainty of the measured beamline flux $F(\hbar\omega)$. All recorded spectra were corrected for detector dark counts, normalized on integration time, sample pressure, and then lateral and spectral quantum efficiencies. The measured relative intensities are called "normalized counts" (n.c.) for brevity. With this procedure, the intensities of all fluorescence lines at different wavelengths and different exciting-photon energies are on the same relative scale.

Three known absolute fluorescence cross sections in neutral atomic nitrogen (Werner 2007) were used for calibration of the normalized counts to an absolute scale. These lines occur after photodissociation of the nitrogen molecule and simultaneous photoexcitation of one of the neutral nitrogen atom fragments with an exciting-photon energy of 25.8 eV. Without changing the geometry of the setup, the intensities of the nitrogen transition at exciting-photon energies, where absolute cross sections are known have been measured. After normalization, a conversion factor was obtained that converts measured normalized counts to an absolute scale. The obtained factors are then applied to the measured adamantane spectra, which have been normalized in the same way. Here it is assumed that the geometry of the interaction volume between synchrotron radiation and target gas as seen by the spectrometer does not change for these different exciting-photon energies. The calibration factors for each transition agree well within their uncertainty margins and are listed in Table 5.

The averaging of these three values was done with a statistical weight on their measured intensities. Hence, the comparatively small intensity and large uncertainty of the peak at 120 nm, close to the lower wavelength sensitivity limit of the usable detector range, have been taken into account. The averaged calibration factor is evaluated to $3.8 \times 10^{-4} \pm 1.1 \times 10^{-4}$ n.c. kbarn^{-1} , with an uncertainty margin of 28.5%.

The statistical experimental uncertainties were propagated, resulting in uncertainty margins in the range of 50%–60%, as indicated by the error bars in Figures 4 and 6.

Table 5
Calibration Factors in Normalized Counts (n.c.) per Kilobarn for Each Peak at the Measured Fluorescence Wavelengths of Nitrogen with an Exciting-photon Energy of 25.8 eV, Calculated from the Absolute Values by Werner (2007)

Position/nm	Cross Section (kbarn)	Meas. Int. (n.c.)	Cal. Factor (n.c. kbarn^{-1})
120.0	18.8 ± 4.1	0.138 ± 0.004	$4.3 \cdot 10^{-4} \pm 1.2 \cdot 10^{-4}$
124.3	10.7 ± 2.4	0.465 ± 0.004	$3.8 \cdot 10^{-4} \pm 1.1 \cdot 10^{-4}$
149.3	44.8 ± 9.9	3.151 ± 0.014	$3.7 \cdot 10^{-4} \pm 1.1 \cdot 10^{-4}$
Mean			$3.8 \cdot 10^{-4} \pm 1.1 \cdot 10^{-4}$

Note. The normalizations have been performed individually for each peak.

ORCID iDs

Lutz Marder https://orcid.org/0000-0001-7293-7589
Philipp Schmidt https://orcid.org/0000-0003-1980-6998
Catmarna Küstner-Wetekam https://orcid.org/0000-0003-4030-516X
Thomas Giesen https://orcid.org/0000-0002-2401-0049
Laurent Nahon https://orcid.org/0000-0001-9898-5693
Andreas Hans https://orcid.org/0000-0002-4176-4766
André Knie https://orcid.org/0000-0002-2208-8838
Arno Ehresmann https://orcid.org/0000-0002-0981-2289

References

Allamandola, L., Sandford, S., Tielens, A., & Herbst, T. 1993, Sci, 260, 64
Bahrdt, J., Frentrup, W., Gaupp, A., et al. 2001, NIMPA, 467, 130
Bauschlicher, C. W., Jr., Liu, Y., Ricca, A., Mattioda, A. L., & Allamandola, L. J. 2007, ApJ, 671, 458
Brault, J. W. 1987, AcMik, 93, 215
Crandall, P. B., Müller, D., Leroux, J., Förstel, M., & Dopfer, O. 2020, ApJL, 900, L20
Dartois, E. 2019, J. Carbon Res., 5, 80
Davidsen, A. F., & Fountain, G. H. 1985, JHATD, 6, 28
De Oliveira, N., Joyeux, D., Roudjane, M., et al. 2016, J. Synchrotron Radiat., 23, 887
De Oliveira, N., Roudjane, M., Joyeux, D., et al. 2011, NaPho, 5, 149
Duley, W. W. 1995, ApJ, 445, 240
Ehresmann, A., Demekhin, P. V., Kielich, W., et al. 2009, JPhB, 42, 165103
Ehresmann, A., Liebel, H., von Kröger, M., & Schmoranzer, H. 2003, JESRP, 130, 49
Ehresmann, A., Werner, L., Klumpp, S., et al. 2004, JPhB, 37, 4405
Filik, J., Harvey, J. N., Allan, N. L., et al. 2006, AcSpA, 64, 681
Glass-Maujean, M., Jungen, Ch., Schmoranzer, H., et al. 2010, PhRvL, 104, 183002
Green, J. C., Froning, C. S., Osterman, S., et al. 2011, ApJ, 744, 60
Hans, A., Knie, A., Schmidt, Ph., et al. 2015, PhRvA, 92, 032511
Hans, A., Schmidt, Ph., Ozga, C., et al. 2018, Mate, 11, 869
Jensen, J. O. 2004, AcSpA, 60, 1895
Jewell, A., Hennessy, J., Jones, T., et al. 2018, Proc. SPIE, 10709, 107090C
Kappe, M., Schiller, A., Krasnokutski, S. A., et al. 2022, PCCP, 24, 23142
Kimble, R. A., Woodgate, B. E., Bowers, C. W., et al. 1997, ApJL, 492, L83
Korolkov, D. V., & Sizova, O. V. 2002, IJQC, 88, 606
Kouchi, A., Nakano, H., Kimura, Y., & Kaito, C. 2005, ApJL, 626, L129
Landt, L., Kielich, W., Wolter, D., et al. 2009a, PhRvB, 80, 205323
Landt, L., Klünder, K., Dahl, J. E., et al. 2009b, PhRvL, 103, 047402
Lebouteiller, V., Yan, C., Gry, H., et al. 2019, arXiv:1909.03056
Lenzke, K., Landt, L., Hoener, M., et al. 2007, JChPh, 127, 084320
Lewis, R. S., Anders, E., & Draine, B. T. 1989, Natur, 339, 117
Liebel, H., Ehresmann, A., Schmoranzer, H., et al. 2002, JPhB, 35, 895
Liebel, H., Lauer, S., Vollweiler, F., et al. 2000, PhLA, 267, 357
Macchetto, F., & Penston, M. V. 1978, ESABu, 13, 9
Maclot, S., Lahl, J., Peschel, J., et al. 2020, NatSR, 10, 2884
Malina, R. F., Bowyer, S., Lampton, M., et al. 1982, OptEn, 21, 764
McIntosh, G. C., Yoon, M., Berber, S., & Tománek, D. 2004, PhRvB, 70, 045401

Muslimov, E., Bouret, J.-C., Neiner, C., et al. 2018, Proc. SPIE, 10699, 1069906
Nahon, L., de Oliveira, N., Garcia, G. A., et al. 2012, J. Synchrotron Radiat., 19, 508
Patrick, C. E., & Giustino, F. 2013, NatCo, 4, 2006
Patzer, A., Schütz, M., Möller, T., & Dopfer, O. 2012, AngCh, 51, 4925
Pirali, O., Boudon, V., Oomens, J., & Vervloet, M. 2012, JChPh, 136, 024310
Pirali, O., Vervloet, M., Dahl, J. E., et al. 2007, ApJ, 661, 919
Polfer, N., Sartakov, B. G., & Oomens, J. 2004, CPL, 400, 201
Raymonda, J. W. 1972, JChPh, 56, 3912
Reichardt, G., Bahrdt, J., Schmidt, J.-S., et al. 2001, NIMPA, 467, 462
Reiß, P., Schmidt, Ph., Tulin, I., et al. 2015, NIMPA, 776, 57
Richter, R., Röhr, M. I. S., Zimmermann, T., et al. 2015, PCCP, 17, 4739
Richter, R., Wolter, D., Zimmermann, T., et al. 2014, PCCP, 16, 3070
Sahnow, D. J., Moos, H. W., Ake, T. B., et al. 2000, ApJL, 538, L7
Schmidt, Ph., Knie, A., Hans, A., et al. 2021, JPhB, 54, 034001
Schwertfeger, H., Fokin, A. A., & Schreiner, P. R. 2008, AngCh, 47, 1022
Shang, Q. Y., & Bernstein, E. R. 1994, JChPh, 100, 8625
Sharipov, F., & Seleznev, V. 1998, JPCRD, 27, 657
Shen, M., Schaefer, H. F., Liang, C., et al. 1992, JAChS, 114, 497
Shustov, B. M., Sachkov, M. E., Sichevsky, S. G., et al. 2021, SoSyR, 55, 677
Solt, K., Melchior, H., Kroth, U., et al. 1996, ApPhL, 69, 3662
Steglich, M., Huisken, F., Dahl, J. E., Carlson, R. M. K., & Henning, Th. 2011, ApJ, 729, 91
Tian, S. X., Kishimoto, N., & Ohno, K. 2002, JPCA, 106, 6541
Vörös, M., Demjén, T., & Gali, A. 2011, MRS Online Proc. Libr., 1370, 23
Vörös, M., & Gali, A. 2009, PhRvB, 80, 161411
Werner, L. 2007, PhD thesis, Univ. of Kassel